Online Resource 1: Supporting Information

Plasmonics

Local Morphology Controls Fano Output Zeros and Nonlinear Chirality in Gold Helicoids

Gürsoy Bozkurt Akgüç[1,2,*], Orion Ciftja[2]

[1]Department of Physics, Izmir University of Economics, Izmir, Türkiye

[2]Department of Physics, Prairie View A&M University, Prairie View, Texas, USA

[*]Corresponding author: gursoy.akguc@ieu.edu.tr

Contents

S1 Purpose and evidence hierarchy **2**

S2 Wavelength and coordinate conventions **3**
S2.1 Pump and SH wavelengths . . . 3
S2.2 Far-field angular circle . . . 3

S3 Computational-domain and export checks **3**
S3.1 Full-sphere complex export . . . 4

S4 Linear connected-face series and diagnostic two-pole fit **4**
S4.1 Complete five-state linear response . . . 4
S4.2 Fit function, representative fits, and diagnostic poles . . . 5

S5 Size, experiment, depth, and connectivity controls **6**
S5.1 Size calibration . . . 6
S5.2 Digitized experimental comparison . . . 6
S5.3 Contained-groove topology and groove-depth controls . . . 7

S6 Scalar far-field metrics **8**
S6.1 Definitions . . . 8
S6.2 Complete scalar results . . . 9

S7 Complex angular-channel analysis **9**
S7.1 Vector Fourier coefficients . . . 9
S7.2 Secondary-channel strength . . . 10
S7.3 Fraction of the fourfold coefficient explained . . . 10

S8 Fixed-channel phase and Argand analysis **10**
S8.1 Why a fixed channel is required . . . 10
S8.2 Argand trajectories . . . 11

S9 Complex singular-value decomposition **11**

S10 Complex overlap of opposite circular-polarization fields **11**

S11 Full-sphere vector-spherical-harmonic decomposition **12**
S11.1 Tangential basis and quadrature . . . 12
S11.2 Multipolar composition and selection family . . . 13
S11.3 Full-sphere fourfold interference coefficient . . . 14

S12 Linear mesh and wavelength convergence **15**

S13 Induced-current phase and overlap diagnostics **17**

S14 Finite collection-angle observables **19**

S15 Damped-oscillator and Fano derivation **19**
S15.1 One oscillator . . . 20
S15.2 Two coupled oscillators . . . 20

S16 Surface-SHG implementation **20**
S16.1 Implemented surface source . . . 20
S16.2 Direct indexed retrieval of the stored pump source . . . 21
S16.3 Radiated SH power and closure . . . 21

S17 Five-state nonlinear spectra: numerical record **21**

S18 Focused nonlinear mesh convergence **22**

S19 Source, overlap, and radiation diagnostics **22**
S19.1 Definitions . . . 22
S19.2 Six-hundred-nanometer hierarchy . . . 23
S19.3 A stronger sign test at $h = -1$, 550 nm . . . 24

S20 Pump-field localization retained only as a pump diagnostic **24**

S21 Spectral connection between linear Fano interference and SHG **26**

S22 Heuristic nonlinear coupled-mode extension **26**

S23 Nonlinear numerical workflow **27**

S24 Radiation-channel and reproducibility scope **27**

S25 Data products in this package **28**

S26 Summary **28**

The companion machine-readable tables are supplied separately as Online Resource 2 (`ESM_2.zip`); paths beginning with `data/` refer to that archive.

S1 Purpose and evidence hierarchy

This Supporting Information documents the numerical conventions, derivations, scalar far-field metrics, complex angular-channel analysis, singular-value decomposition, full-sphere vector-spherical-harmonic (VSH) decomposition, nonlinear implementation, and reproducibility requirements underlying the main manuscript. The evidence is separated into six levels:

1. **full-wave scalar exports**: linear scattering/absorption and SH powers;
2. **equatorial full-wave complex exports**: complex Cartesian far-field components on a fixed azimuthal circle;
3. **full-sphere complex exports**: complex Cartesian far fields on the spherical angular grid for all five geometries, wavelengths, and polarizations;
4. **derived complex observables**: angular Fourier coefficients, fixed-channel phase, Argand trajectories, SVD channels, full-sphere C_4, and VSH multipole coefficients;
5. **derived scalar observables**: g factors, anisotropy, fourfold strength, shape differences, multipolar power fractions, and interference visibility;
6. **reduced models**: diagnostic two-pole amplitudes and nonlinear Fano equations.

The first five levels are direct calculations or algebraic postprocessing of numerical fields. The reduced model is an interpretation. The radiation-multipole assignment is established from the full sphere; no one-to-one mapping between radiation channels and open-system eigenmodes is assumed.

Figures shown in the main text are not repeated here. The Supporting Information contains only additional controls, validation plots, numerical tables, derivations, phase quadratures, refinement tests, and finite-collection diagnostics. Size calibration, the digitized experimental comparison, groove-depth/connectivity controls, pole trajectories, full-sphere validation/composition, signed

normal-field maps, convergence/current diagnostics, and the finite-NA tradeoff are included because they constrain the interpretation independently.

S2 Wavelength and coordinate conventions

Polarization labels and the dissymmetry sign convention are defined once in the main manuscript. The Supporting Information uses LCP/RCP directly; the numerical `pol` parameter is retained only where needed to reproduce COMSOL solution retrieval.

S2.1 Pump and SH wavelengths

The nonlinear sweep uses

$$\lambda_\omega = 1080, 1090, \ldots, 1640 \text{ nm}, \tag{S1}$$

and results are plotted against

$$\lambda_{2\omega} = \frac{\lambda_\omega}{2} = 540, 545, \ldots, 820 \text{ nm}. \tag{S2}$$

All nonlinear wavelengths in the tables refer to $\lambda_{2\omega}$ unless "pump" is written explicitly.

S2.2 Far-field angular circle

The far-field cut has normal vector $\hat{\boldsymbol{z}}$ and reference direction $\hat{\boldsymbol{x}}$. Thus $\phi = 0$ corresponds to $+x$, 90° to $+y$, and the observation direction is

$$\hat{\boldsymbol{n}}(\phi) = (\cos\phi, \sin\phi, 0). \tag{S3}$$

The transverse basis is

$$\hat{\boldsymbol{e}}_\phi = (-\sin\phi, \cos\phi, 0), \tag{S4}$$

$$\hat{\boldsymbol{e}}_\theta = (0, 0, -1), \tag{S5}$$

which gives

$$E_\phi = -E_x^{\text{far}} \sin\phi + E_y^{\text{far}} \cos\phi, \tag{S6}$$

$$E_\theta = -E_z^{\text{far}}. \tag{S7}$$

S3 Computational-domain and export checks

Full-wave calculations were performed with COMSOL Multiphysics 6.4 and the Wave Optics Module (COMSOL AB, Stockholm, Sweden). The nominal particle size is 160 nm and the host refractive index is $n_h = 1.3$. Gold dispersion follows the Johnson–Christy optical constants [1].

The far-field integration boundary and outer PML boundary are at 400 and 550 nm from the particle center. The complex far-field files contain 28,158 rows per geometry:

$$39 \text{ wavelengths} \times 2 \text{ polarizations} \times 361 \text{ angles}. \tag{S8}$$

The first and last angles correspond to 0 and 2π; the latter is removed before averaging to avoid double weighting.

The exported far-field norm was checked against the complex components,

$$E_{\text{norm}} = \sqrt{|E_x^{\text{far}}|^2 + |E_y^{\text{far}}|^2 + |E_z^{\text{far}}|^2}. \tag{S9}$$

The maximum relative reconstruction error was 3.9–4.2 $\times 10^{-16}$ for the five files; the file-by-file validation is collected in Table S1.

Table S1: Complex far-field export validation.

h	rows	wavelength range	wavelengths per polarization	max relative norm error
−1	28158	540–820 nm	39	4.16×10^{-16}
−0.5	28158	540–820 nm	39	3.87×10^{-16}
0	28158	540–820 nm	39	3.98×10^{-16}
+0.5	28158	540–820 nm	39	4.07×10^{-16}
+1	28158	540–820 nm	39	4.07×10^{-16}

S3.1 Full-sphere complex export

The second COMSOL export contains the complex Cartesian far field for all five geometries. Each parameter state contains 2631 radiation-pattern nodes. The interior sphere is a tensor grid of 35 polar rings (5°–175° in 5° increments) and 73 uniformly spaced azimuthal samples; COMSOL stores pole samples separately. With 39 wavelengths and two polarizations, each geometry contains 205,218 data rows. The physical field is transverse to numerical precision:

$$\max \frac{|\hat{\boldsymbol{r}} \cdot \boldsymbol{E}_{\mathrm{far}}|}{|\boldsymbol{E}_{\mathrm{far}}|} < 8.6 \times 10^{-15} \tag{S10}$$

over all five files.

The stored visible wavelengths are the 39 parametric solutions used in the linear study; several values in the export are integer-rounded representations of the refined local wavelength list. The broad maximum is exported near 729 nm and is referred to as approximately 730 nm in the text.

S4 Linear connected-face series and diagnostic two-pole fit

S4.1 Complete five-state linear response

The five-state scattering-dissymmetry trajectory is shown in the main manuscript; the quantitative production-spectrum extrema are collected here. The helicoid backbone and five unmodified faces remain left-handed throughout the series. The selected face is left-handed at $h = +1$, reduced in left-handed winding at $h = +0.5$, radial at $h = 0$, partially right-handed at $h = -0.5$, and fully right-handed counter-wound at $h = -1$. The intermediate states are numerically essential: the strongest negative scattering dissymmetry occurs at $h = -0.5$, not at the fully counter-wound endpoint, while the largest positive branch occurs at $h = 0$. Thus the linear trajectory is intrinsically non-monotonic rather than an interpolation between the two endpoint geometries.

Table S2: Validated extrema of the production linear scattering-dissymmetry spectra for the edge-connected five-state series.

h	$g_{\mathrm{sca}}^{\mathrm{min}}$	wavelength	$g_{\mathrm{sca}}^{\mathrm{max}}$	wavelength
+1	−0.1774	585 nm	+0.1065	620 nm
+0.5	−0.2039	580 nm	+0.1090	615 nm
0	−0.2363	580 nm	+0.1169	610 nm
−0.5	−0.2749	585 nm	+0.1111	620 nm
−1	−0.2730	585 nm	+0.0881	630 nm

Table S2 gives the production scattering extrema. The corresponding absorption and extinction extrema are included in the machine-readable file `data/complete_edge_connected_h_series_extrema.csv`. The independent full-sphere integration used for the main-text scattering curve is supplied as `data/linear_gsca_fullsphere_reconstruction.csv`; it reproduces the same non-monotonic trajectory and provides a direct consistency check between the scalar cross-section calculation and the complex far-field export.

S4.2 Fit function, representative fits, and diagnostic poles

For $E = hc/\lambda$, the four raw channels of one geometry were fit simultaneously with

$$\sigma_{c,s}(E) = S_{c,s}\left|b_{c,s} + \frac{R_{b,c,s}}{E - E_b + \mathrm{i}\Gamma_b} + \frac{R_{d,c,s}}{E - E_d + \mathrm{i}\Gamma_d}\right|^2, \tag{S11}$$

where $c \in \{\mathrm{sca}, \mathrm{abs}\}$. The pole positions and widths are shared among the four channels, whereas the backgrounds and complex residues are channel specific. Multiple bounded least-squares initializations were used, and the normalized channel errors were approximately 2–4%.

Table S3: Diagnostic intensity-fit pole parameters.

h	broad E (eV)	broad Γ (eV)	narrow E (eV)	narrow Γ (eV)
+1	2.0520	0.2303	1.7122	0.0763
+0.5	2.0685	0.2475	1.7206	0.0722
0	2.0684	0.2481	1.7218	0.0721
−0.5	2.0671	0.2390	1.7195	0.0754
−1	2.0606	0.2519	1.7156	0.0801

Table S3 lists the fitted broad and narrow pole parameters used in this diagnostic representation.

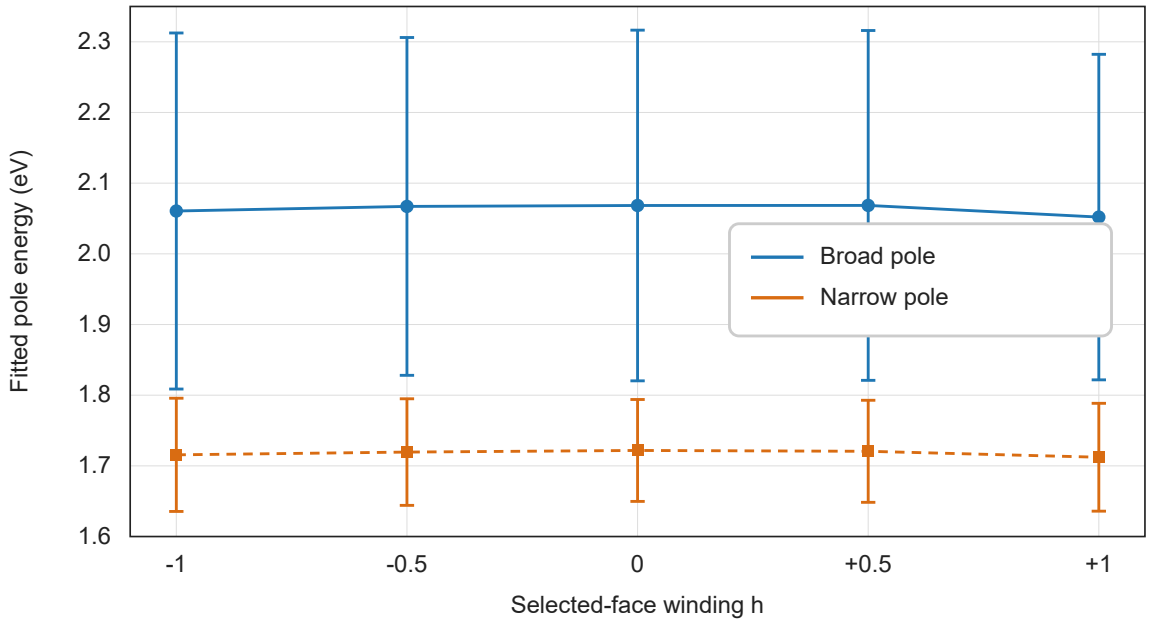


Figure S1: The fitted intensity-spectrum pole locations move only modestly with h. The larger changes in dissymmetry are consistent with changes in complex residues, backgrounds, and output zeros. Bars show the fitted half-widths Γ listed in Table S3, not statistical uncertainties in the pole energies. The fitted poles are diagnostic rather than unique eigenmode identifications.

Figure S1 makes clear that the fitted pole locations move only modestly over the five-state trajectory.

Because the scalar fit is used only as a diagnostic representation, the fitted pole values are not interpreted as unique quasinormal-mode parameters.

S5 Size, experiment, depth, and connectivity controls

S5.1 Size calibration

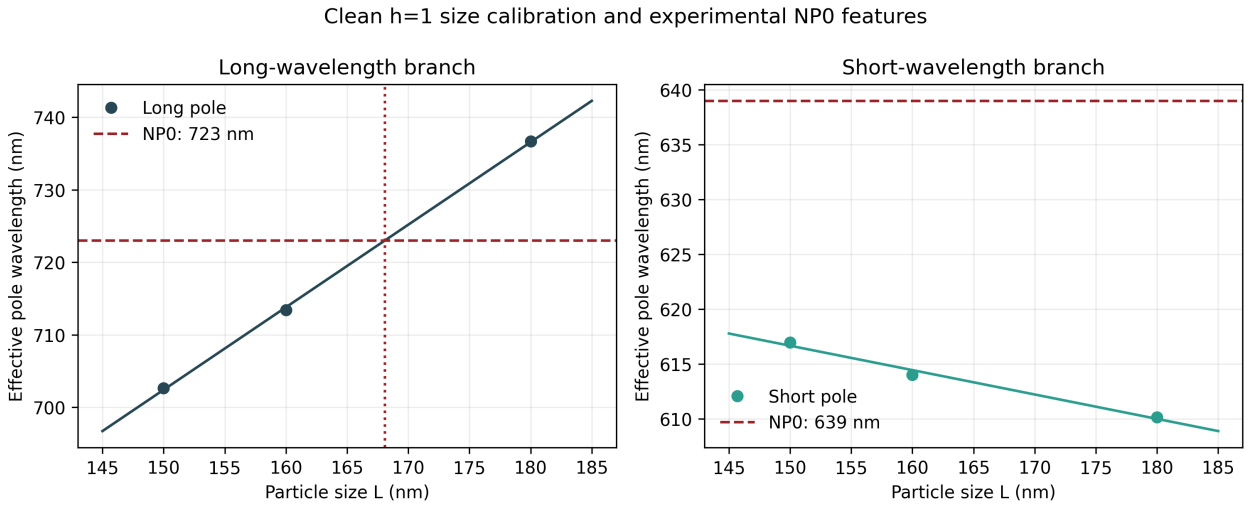


Figure S2: Size calibration for the clean $h = +1$ geometry. The long-wavelength effective pole crosses the experimental 723 nm feature near a nominal size of 168 nm, while the short-wave branch shifts in the opposite direction and does not reach the experimental feature near 640 nm over the tested 150–180 nm interval.

Figure S2 summarizes the size sweep. The size sweep supplies a useful negative result: uniform rescaling cannot align both experimental features simultaneously. Geometry mixing, local groove parameters, environmental corrections, or mode coupling are therefore required in addition to size calibration.

S5.2 Digitized experimental comparison

The NP0 experimental intensities digitized for this diagnostic comparison are taken from Spreyer *et al.* [2]; the digitization is used only to compare broad spectral landmarks. Figure S3 shows the corresponding diagnostic fit.

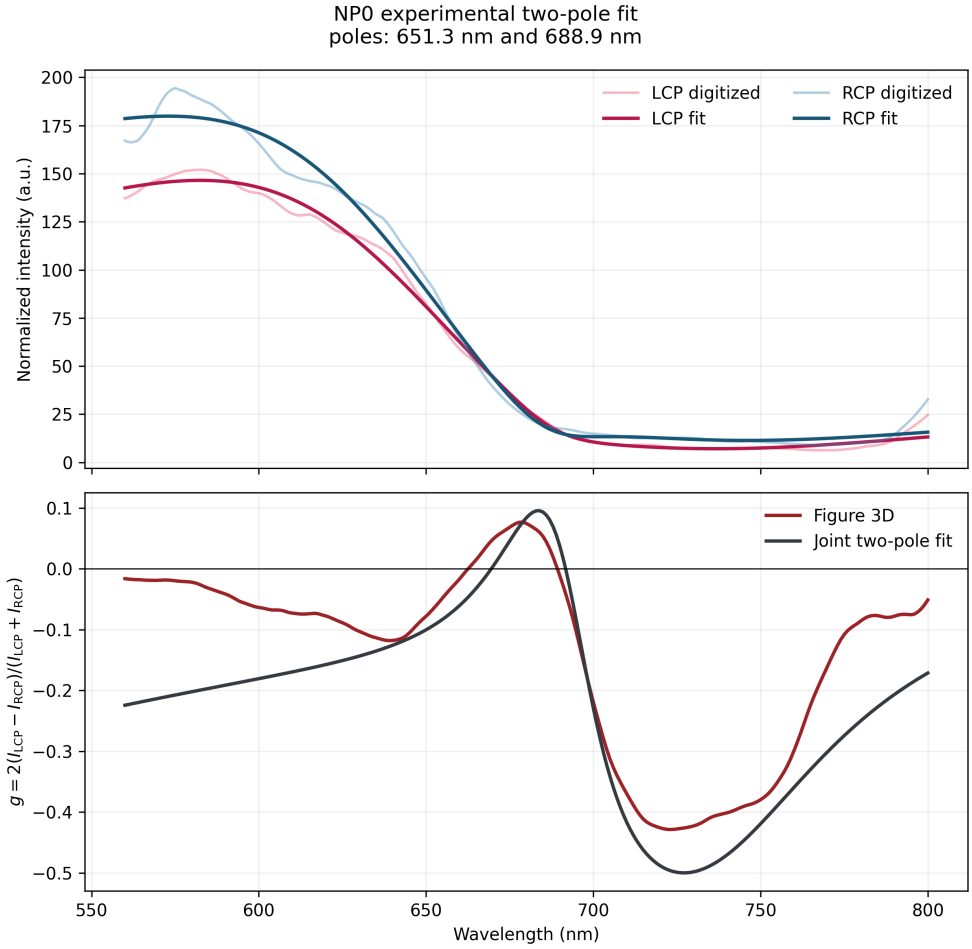


Figure S3: Diagnostic two-pole fit to digitized NP0 experimental intensities from Spreyer *et al.* [2]. It captures the broad dissymmetry structure but remains phenomenological; digitization uncertainty remains.

S5.3 Contained-groove topology and groove-depth controls

Face helicity h, normalized groove depth D, and edge connectivity C are treated as independent geometry coordinates,

$$\boldsymbol{p}_{\mathrm{geom}} = (h, D, C), \qquad D = d_{\max}/(27\ \mathrm{nm}). \tag{S12}$$

The main five-state series uses edge-connected grooves so that current pathways can continue across neighboring rounded faces. Earlier topology controls instead terminate the groove mouths before the rounded edges. These contained geometries are useful controls rather than discarded prototypes: they isolate how inter-face continuity changes the optical response while preserving the same overall helicoid scale and comparable groove winding.

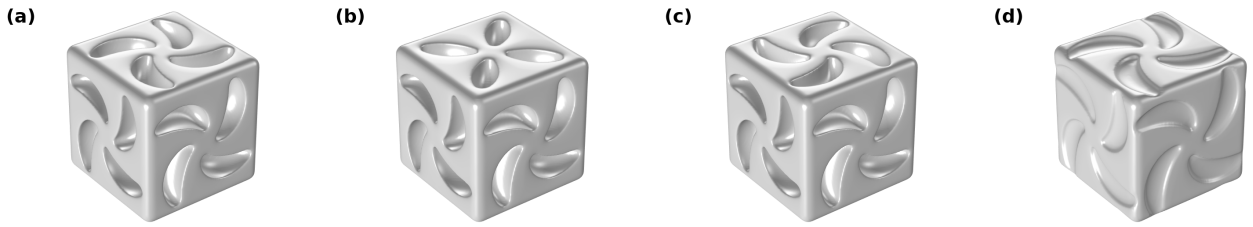


Figure S4: Geometry controls used to separate selected-face winding, edge connectivity, and groove depth. Panels (a–c) show the contained-groove $D = 1$ family with (a) the reference-like $h = +1$ face, (b) the radial $h = 0$ face, and (c) the counter-wound $h = -1$ face; in these three cases the groove mouths terminate before the rounded cube edges. Panel (d) shows the shallow edge-touching V21C control, for which the reference winding is retained but the groove depth is reduced to $D = 0.25$ (maximum depth 6.75 nm) while the grooves approach the rounded edges.

The clean $h = +1$ comparison is especially informative. The polarization-averaged scattering peak is nearly unchanged by connectivity: $\langle\sigma_{sca}\rangle_{max} = 0.2171\ \mu m^2$ at 720 nm for the contained geometry and $0.2139\ \mu m^2$ at 730 nm for the connected geometry. The helicity contrast, however, is strongly reorganized. The contained reference has $g_{sca}^{max} = +0.06848$ at 580 nm and $g_{sca}^{min} = -0.04888$ at 620 nm, whereas the connected reference reaches +0.10647 at 620 nm and −0.17745 at 585 nm. Edge connectivity therefore changes the interference between helicity-selective radiation channels far more strongly than it changes the gross scattering resonance.

The radial-face control shows the same sensitivity from another direction. A contained diagonal $h = 0$ face reaches only $g_{sca}^{max} = +0.01196$ at 595 nm, whereas allowing the radial grooves to spill across the rounded edges produces $g_{sca}^{max} = +0.17717$ at 590 nm and $g_{sca}^{min} = -0.04040$ at 630 nm. Groove depth is an independent coordinate. The shallow edge-touching V21C geometry shown in Fig. S4(d) retains the reference winding but reduces the maximum groove depth from 27 nm to 6.75 nm ($D = 0.25$). It still supports a strong polarization-averaged scattering resonance, $\langle\sigma_{sca}\rangle_{max} = 0.2071\ \mu m^2$ near 660 nm, while the helicity-resolved scattering curves become nearly indistinguishable: $g_{sca}^{max} = +3.89 \times 10^{-4}$ and $g_{sca}^{min} = -2.611 \times 10^{-3}$. Thus the suppression of dissymmetry is not caused by disappearance of the plasmonic resonance; strong resonance and strong dissymmetry are not synonymous.

A deeper contained reference geometry with $D = 1.25$ was also generated with the original non-edge-touching radial extent and passed the cutter-overlap geometry check. No optical spectrum from that control is used in the present analysis; it is retained in Table S4 only to document the independent depth coordinate rather than to imply an additional spectral result.

Table S4: Topology and groove-depth controls. The controls are kept separate from the main five-state h sequence because connectivity and/or groove depth differ.

Case	D	edge condition	established result
Contained $h = +1$	1.00	contained	$\langle\sigma_{sca}\rangle_{max} = 0.2171\ \mu m^2$ at 720 nm; $g_{sca}^{max} = +0.06848$ at 580 nm; $g_{sca}^{min} = -0.04888$ at 620 nm
Connected $h = +1$	1.00	connected	$\langle\sigma_{sca}\rangle_{max} = 0.2139\ \mu m^2$ at 730 nm; $g_{sca}^{max} = +0.10647$ at 620 nm; $g_{sca}^{min} = -0.17745$ at 585 nm
Contained diagonal $h = 0$	1.00	contained	$g_{sca}^{max} = +0.01196$ at 595 nm
Axis-aligned $h = 0$	1.00	edge-spilling	$g_{sca}^{max} = +0.17717$ at 590 nm and $g_{sca}^{min} = -0.04040$ at 630 nm
V21C, $h = +1$	0.25	edge-touching	$\langle\sigma_{sca}\rangle_{max} = 0.2071\ \mu m^2$ near 660 nm; $\lvert g_{sca}\rvert < 0.003$ over the reported control range
Deep contained V22B	1.25	contained	geometry and cutter-overlap check only; no optical spectrum is used here

S6 Scalar far-field metrics

S6.1 Definitions

The intensity proxy on the angular cut is

$$I(\phi, \lambda) = |E_\theta|^2 + |E_\phi|^2. \tag{S13}$$

The mean planar intensity is

$$M_0 = \frac{1}{2\pi}\int_0^{2\pi} I(\phi)\, d\phi. \tag{S14}$$

The angular anisotropy is a coefficient of variation,

$$A_{ang} = \frac{\sqrt{\langle (I - M_0)^2\rangle_\phi}}{M_0}. \tag{S15}$$

The normalized complex Fourier coefficient of the intensity is

$$Z_n = \frac{\langle I(\phi) e^{-in\phi}\rangle_\phi}{M_0}, \tag{S16}$$

and the fourfold strength is

$$F_4 = |Z_4|. \tag{S17}$$

Its orientation is $\phi_4 = \arg Z_4/4$ modulo 90°.

The planar dissymmetry is

$$g_{\mathrm{plane}} = 2\frac{M_{0,\mathrm{LCP}} - M_{0,\mathrm{RCP}}}{M_{0,\mathrm{LCP}} + M_{0,\mathrm{RCP}}}. \tag{S18}$$

The normalized pattern difference is

$$D_{\mathrm{shape}} = \sqrt{\left\langle \left(\frac{I_{\mathrm{LCP}}}{M_{0,\mathrm{LCP}}} - \frac{I_{\mathrm{RCP}}}{M_{0,\mathrm{RCP}}} \right)^2 \right\rangle_{\phi}}. \tag{S19}$$

Unlike g_{plane}, D_{shape} is insensitive to a common multiplicative difference between the two patterns.

S6.2 Complete scalar results

The corresponding all-h scalar summary figure is shown in the main manuscript and is not repeated here. Numerical extrema and definitions are given below.

Table S5: Extrema of the scalar angular metrics.

h	$A_+^{\max}$	λ	$A_-^{\max}$	λ	$F_{4,+}^{\max}$	λ	$F_{4,-}^{\max}$	λ
−1	0.1759	575	0.2166	585	0.1223	575	0.1513	585
−0.5	0.1568	555	0.2318	590	0.1096	555	0.1618	590
0	0.1832	595	0.2407	590	0.1278	595	0.1683	590
+0.5	0.1926	595	0.2293	590	0.1345	595	0.1601	590
+1	0.1860	600	0.2028	595	0.1299	600	0.1413	595

Table S5 collects the extrema of the scalar angular metrics.

Table S6: LCP/RCP shape and planar-intensity extrema.

h	$D_{\mathrm{shape}}^{\max}$	wavelength	$g_{\mathrm{plane}}^{\min}$	$g_{\mathrm{plane}}^{\max}$
−1	0.2978	575 nm	−0.2024 at 590 nm	+0.0711 at 625 nm
−0.5	0.3132	585 nm	−0.1761 at 585 nm	+0.0688 at 615 nm
0	0.3611	585 nm	−0.1236 at 580 nm	+0.0516 at 610 nm
+0.5	0.3583	585 nm	−0.0961 at 585 nm	+0.0276 at 610 nm
+1	0.3206	590 nm	−0.0878 at 590 nm	+0.0155 at 760 nm

Table S6 gives the complementary LCP/RCP pattern-shape and planar-intensity extrema.

For every geometry and polarization, the planar mean intensity peaks at 730 nm. The stability of this broad maximum contrasts with the short-band variation of A_{ang}, F_4, and D_{shape}.

S7 Complex angular-channel analysis

S7.1 Vector Fourier coefficients

The complex transverse field is expanded as

$$\boldsymbol{e}(\phi) = \sum_m \boldsymbol{c}_m e^{im\phi}, \qquad \boldsymbol{c}_m = \frac{1}{2\pi}\int_0^{2\pi} \boldsymbol{e}(\phi) e^{-im\phi}\, d\phi. \tag{S20}$$

Here m is the integer azimuthal Fourier index of the radiated field, while σ denotes the incident circular-polarization index defined in the main manuscript. The fourfold geometry organizes the observed azimuthal orders into the family

$$m = \sigma + 4q, \qquad q \in \mathbb{Z}. \tag{S21}$$

The dominant coefficients are the principal member $m = \sigma$ and the nearest important secondary member $m = -3\sigma$, corresponding to $q = -\sigma$. Thus the dominant pair is $(m = -1, +3)$ for LCP and $(m = +1, -3)$ for RCP. Their index difference is four, which produces the fourfold interference term. With only these terms,

$$\boldsymbol{e} = \boldsymbol{c}_{\sigma} e^{\mathrm{i}\sigma\phi} + \boldsymbol{c}_{-3\sigma} e^{-\mathrm{i}3\sigma\phi}, \tag{S22}$$

$$I = |\boldsymbol{c}_{\sigma}|^2 + |\boldsymbol{c}_{-3\sigma}|^2 + 2\,\mathrm{Re}\left[\boldsymbol{c}_{\sigma} \cdot \boldsymbol{c}^{*}_{-3\sigma} e^{\mathrm{i}4\sigma\phi}\right]. \tag{S23}$$

Thus the fourfold intensity coefficient is produced by the complex inner product of the two vector coefficients. This is important: the lobe orientation and contrast depend on both the amplitude ratio and the polarization-vector phase.

S7.2 Secondary-channel strength

The corresponding complex angular-channel figure is shown in the main manuscript and is not repeated here.

Table S7: Maximum secondary-to-dominant amplitude ratios.

h	$r^{\max}_{\mathrm{LCP}}$	wavelength	$r^{\max}_{\mathrm{RCP}}$	wavelength
−1	0.1577	585 nm	0.1263	560 nm
−0.5	0.1711	590 nm	0.1203	600 nm
0	0.1829	590 nm	0.1458	595 nm
+0.5	0.1753	590 nm	0.1521	595 nm
+1	0.1526	600 nm	0.1456	600 nm

Table S7 shows that the secondary angular channel remains small in amplitude despite its strong interference effect.

At these maxima, the secondary power fraction within the two-channel subspace is $r^2/(1 + r^2) \simeq 1.4$–3.2%. Its interference contribution is much larger because it is linear in r.

S7.3 Fraction of the fourfold coefficient explained

Let

$$I_{4,\mathrm{meas}} = \langle I e^{-\mathrm{i}4\sigma\phi} \rangle_{\phi}, \tag{S24}$$

and

$$I_{4,\mathrm{pair}} = \boldsymbol{c}^{\dagger}_{-3\sigma} \boldsymbol{c}_{\sigma}. \tag{S25}$$

The ratio $|I_{4,\mathrm{pair}}|/|I_{4,\mathrm{meas}}|$ has median values between approximately 0.983 and 0.992 across the five geometries and two incident polarizations. The residual fourfold coefficient comes from weaker angular harmonics and numerical discretization.

S8 Fixed-channel phase and Argand analysis

S8.1 Why a fixed channel is required

The main-text fixed-channel and Argand figures are not repeated here; this section retains the definitions and complete numerical tables.

A wavelength-dependent direction of maximum radiation cannot be used for phase tracking because the detector itself would move through the angular field. We therefore choose E_θ at $\phi = 0$ for every wavelength. Equivalent checks at several fixed directions show the same short-band behavior.

For the complex amplitude $A(\lambda)$,

$$|A| = \sqrt{(\mathrm{Re}\,A)^2 + (\mathrm{Im}\,A)^2}, \tag{S26}$$

$$\varphi_A = \mathrm{atan2}(\mathrm{Im}\,A, \mathrm{Re}\,A), \tag{S27}$$

with phase unwrapped along the wavelength axis.

Table S8: Fixed-channel Fano indicators. The dip ratio is the minimum amplitude divided by the median amplitude over 540–650 nm.

h	σ	dip wavelength	dip ratio	$\Delta\varphi_{570\to610}$	phase range 540–650
−1	−1	595 nm	0.279	−1.265	see CSV
−1	+1	585 nm	0.147	−1.695	see CSV
−0.5	−1	590 nm	0.324	−1.227	see CSV
−0.5	+1	585 nm	0.129	−1.563	see CSV
0	−1	590 nm	0.428	−1.107	see CSV
0	+1	585 nm	0.282	−1.371	see CSV
+0.5	−1	590 nm	0.472	−1.054	see CSV
+0.5	+1	585 nm	0.283	−1.337	see CSV
+1	−1	595 nm	0.403	−1.084	see CSV
+1	+1	590 nm	0.166	−1.401	see CSV

Table S8 collects the fixed-channel amplitude minima and phase-rotation indicators for all five geometries.

The sign of the phase change is convention dependent. Its magnitude and spectral localization are the physically relevant observations.

S8.2 Argand trajectories

The corresponding Argand trajectories are shown in the main manuscript and are not repeated here. A resonant pole produces a curved trajectory in the complex plane. A broad background plus a narrower resonant contribution can cause the total amplitude to approach the origin. The present trajectories approach the origin near 585–595 nm and then leave with a rotated phase. Because the amplitude does not cross exactly through zero, the phase variation is finite rather than an ideal discontinuous π jump.

S9 Complex singular-value decomposition

The low-rank trend figure is shown in the main manuscript and is not repeated here.

For each geometry and incident polarization, define a matrix

$$\boldsymbol{M} = \begin{pmatrix} E_\theta(\phi_1,\lambda_1) & \cdots & E_\theta(\phi_1,\lambda_N) \\ \vdots & & \vdots \\ E_\theta(\phi_M,\lambda_1) & \cdots & E_\theta(\phi_M,\lambda_N) \\ E_\phi(\phi_1,\lambda_1) & \cdots & E_\phi(\phi_1,\lambda_N) \\ \vdots & & \vdots \end{pmatrix}. \tag{S28}$$

Its SVD is $\boldsymbol{M} = \boldsymbol{U}\boldsymbol{\Sigma}\boldsymbol{V}^\dagger$. The energy fraction of singular channel k is

$$f_k = \frac{\sigma_k^2}{\sum_j \sigma_j^2}. \tag{S29}$$

Table S9 quantifies the resulting two-channel low-rank structure across the five-state series.

Two complex channels are therefore sufficient without assuming an angular Fourier basis. The third singular channel is two orders of magnitude smaller than the second.

S10 Complex overlap of opposite circular-polarization fields

A normalized complex vector overlap was also calculated,

$$\Gamma_{\mathrm{LR}} = \frac{\int (E_{\theta,\mathrm{LCP}} E^*_{\theta,\mathrm{RCP}} + E_{\phi,\mathrm{LCP}} E^*_{\phi,\mathrm{RCP}})\, d\phi}{\sqrt{\int (|E_{\theta,\mathrm{LCP}}|^2 + |E_{\phi,\mathrm{LCP}}|^2)\, d\phi \int (|E_{\theta,\mathrm{RCP}}|^2 + |E_{\phi,\mathrm{RCP}}|^2)\, d\phi}}. \tag{S30}$$

Table S9: SVD results in the 560–630 nm interaction window.

h	σ	f_2	$f_1 + f_2$	f_3
−1	−1	0.03107	0.999851	0.000147
−1	+1	0.03056	0.999817	0.000181
−0.5	−1	0.02066	0.999732	0.000266
−0.5	+1	0.02505	0.999624	0.000374
0	−1	0.01222	0.999799	0.000200
0	+1	0.01598	0.999591	0.000408
+0.5	−1	0.00966	0.999806	0.000192
+0.5	+1	0.01485	0.999596	0.000403
+1	−1	0.01202	0.999613	0.000383
+1	+1	0.02112	0.999570	0.000428

Its magnitude is of order 10^{-3}. This quantity is not used as a principal Fano metric because opposite incident helicities naturally produce nearly orthogonal complex polarization states even when their scalar intensity patterns look similar. The fixed-output-component phase and the internal angular-channel phase are more informative.

S11 Full-sphere vector-spherical-harmonic decomposition

S11.1 Tangential basis and quadrature

Following standard electromagnetic multipole practice [3], for the usual scalar spherical harmonic $Y_{\ell m}$ we define the tangential vector harmonics

$$\boldsymbol{\Psi}_{\ell m} = \frac{r\nabla Y_{\ell m}}{\sqrt{\ell(\ell+1)}}, \tag{S31}$$

$$\boldsymbol{\Phi}_{\ell m} = \hat{\boldsymbol{r}} \times \boldsymbol{\Psi}_{\ell m}. \tag{S32}$$

The complex far field is written

$$\boldsymbol{E}_{\text{far}} = \sum_{\ell m} \left[a^{(E)}_{\ell m} \boldsymbol{\Psi}_{\ell m} + a^{(M)}_{\ell m} \boldsymbol{\Phi}_{\ell m} \right]. \tag{S33}$$

A z-directed electric dipole projects onto $\boldsymbol{\Psi}_{10}$ and a z-directed magnetic dipole onto $\boldsymbol{\Phi}_{10}$, fixing the electric/magnetic naming convention used here. The projection uses composite Simpson weights on the 5° polar grid and periodic equal weights on the 73-point azimuthal grid. Pole samples have zero $\sin\theta$ weight. To remove the small non-orthogonality introduced by finite sampling, the coefficient vector is obtained from

$$\boldsymbol{G}\boldsymbol{a} = \boldsymbol{b}, \qquad G_{\alpha\beta} = \sum_i w_i \boldsymbol{B}^*_\alpha(\Omega_i) \cdot \boldsymbol{B}_\beta(\Omega_i), \qquad b_\alpha = \sum_i w_i \boldsymbol{B}^*_\alpha(\Omega_i) \cdot \boldsymbol{E}_{\text{far}}(\Omega_i). \tag{S34}$$

The discrete Gram matrix differs from the identity by less than 10^{-3} for $\ell_{\max} = 8$.

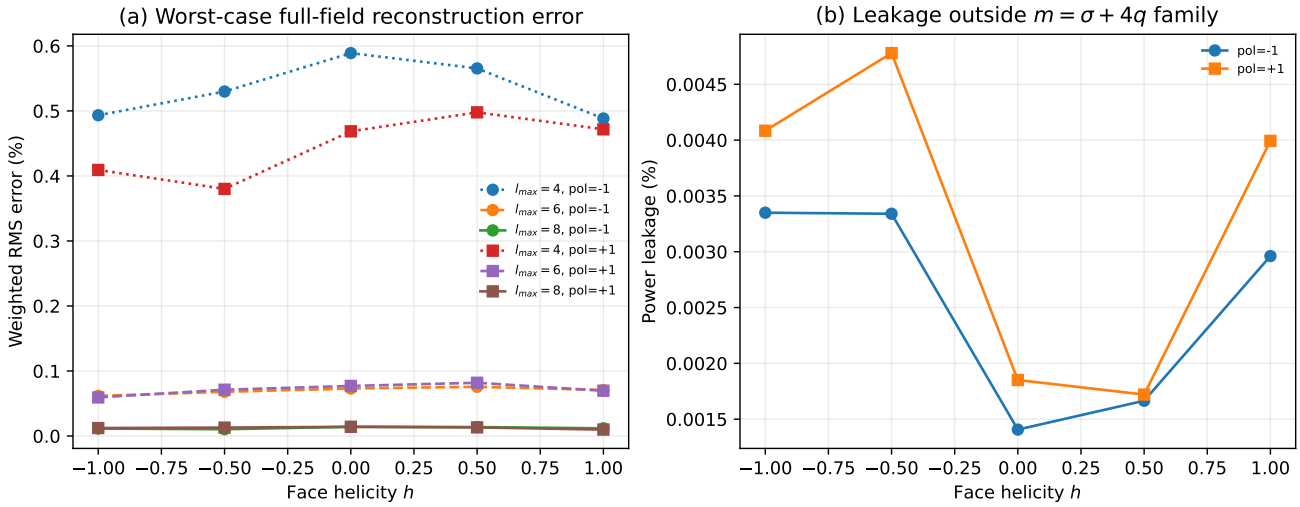


Figure S5: Numerical validation of the full-sphere decomposition. (a) Worst reconstruction error for $\ell_{\max} = 4, 6, 8$ across wavelength for each geometry and polarization. The global $\ell_{\max} = 8$ maximum is 1.42×10^{-4}. (b) Leakage outside the observed $m = \sigma + 4q$ family; the largest leakage is below 4.8×10^{-3}%.

Figure S5 documents the reconstruction and truncation stability of the full-sphere VSH analysis.

S11.2 Multipolar composition and selection family

For each coefficient the reported radiated-power fraction is $|a_{\ell m}^{(E/M)}|^2/P_{\text{far}}$; the finite-grid Gram correction changes the summed fraction by less than the reconstruction uncertainty. More than 99.995% of the resolved power lies in

$$m = \sigma + 4q. \tag{S35}$$

The full-sphere result therefore confirms that the equatorial $m = \sigma$ and $m = -3\sigma$ channels are not artifacts of a single plane. For LCP these are $m = -1$ and $m = +3$; for RCP they are $m = +1$ and $m = -3$.

Table S10: Peak power in the secondary $m = -3\sigma$ family and its electric-octupole component. Percentages are relative to total full-sphere radiated power.

h	σ	max secondary (%)	wavelength	$E, \ell = 3, m = -3\sigma$ (%)
+1	−1	0.925	600 nm	0.842
+0.5	−1	1.155	590 nm	1.064
0	−1	1.268	590 nm	1.179
−0.5	−1	1.145	590 nm	1.061
−1	−1	0.967	590 nm	0.886
+1	+1	0.937	605 nm	0.865
+0.5	+1	0.978	600 nm	0.905
0	+1	0.914	600 nm	0.841
−0.5	+1	0.660	605 nm	0.601
−1	+1	0.553	555 nm	0.533

Table S10 quantifies the electric-octupole content of the weak $m = -3\sigma$ family.

The secondary branch is therefore predominantly electric octupole. For $h = -1$ under RCP illumination, the global maximum moves to the short-wave side near 555 nm; the approximately 600 nm branch is instead suppressed to roughly 0.4%, so this case is better described as a branch restructuring than as a simple resonance shift.

At 590 nm and $h = 0$ under LCP illumination, the total electric-dipole, electric-quadrupole, magnetic-dipole, and electric-$\ell = 3$ fractions are approximately 73.39, 15.03, 9.28, and 1.98%, respectively. The specific electric-octupole coefficient $(\ell, m) = (3, +3)$

carries 1.179%. Near 729 nm the same geometry is approximately 57.97% electric dipole, 41.54% electric quadrupole, and 0.40% magnetic dipole for LCP. Thus the broad long-wave radiation is not a pure dipole resonance but a coherent ED/EQ mixture.

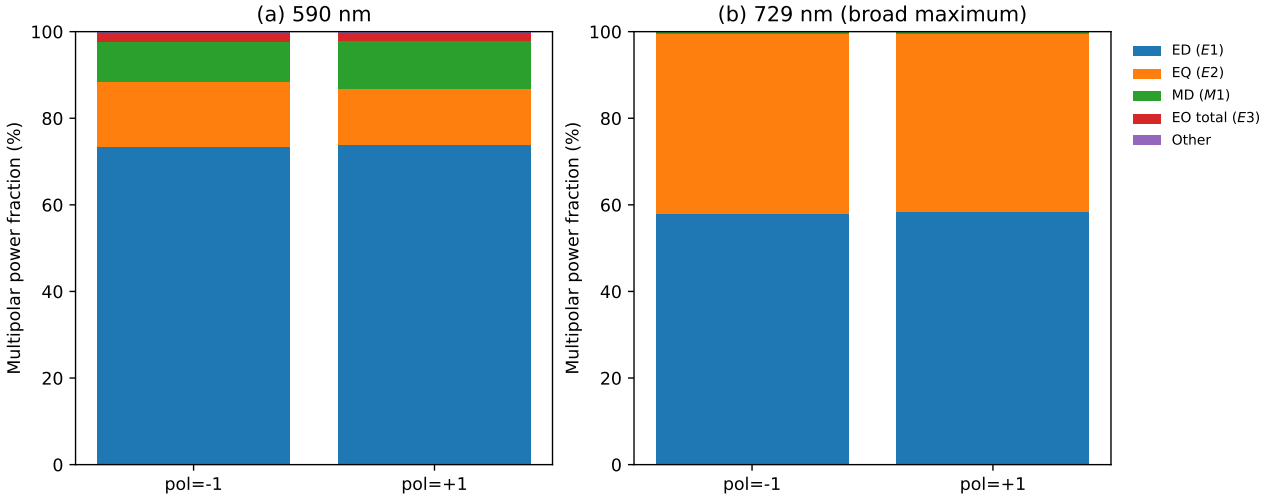


Figure S6: Representative full-sphere multipolar composition for $h = 0$. The structured 590 nm band contains substantial ED, EQ, and MD radiation plus the weak electric-octupolar branch. Near the broad maximum, the radiation is almost entirely ED/EQ.

Figure S6 shows a representative multipolar composition in the structured and broad spectral regions.

S11.3 Full-sphere fourfold interference coefficient

Define

$$C_4^{(\sigma)}(\lambda) = \frac{\int I(\theta,\phi,\lambda) e^{-\mathrm{i}4\sigma\phi}\, d\Omega}{\int I(\theta,\phi,\lambda)\, d\Omega}, \qquad V_4 = 2|C_4|. \tag{S36}$$

V_4 is the normalized amplitude of the fourfold angular modulation associated with the coherent $m = \sigma/m = -3\sigma$ pair. It is not presented as a unique scalar Fano q because the system is vectorial and lossy and the two m families are orthogonal in the fully angle-integrated power.

Table S11: Peak full-sphere interference visibility in 570–620 nm and phase change of C_4 from 570 to 610 nm.

h	σ	max V_4 (%)	wavelength	$\Delta \arg C_4$ (rad)
+1	−1	9.82	600 nm	−0.592
+0.5	−1	10.89	590 nm	−0.876
0	−1	11.53	590 nm	−0.935
−0.5	−1	11.21	590 nm	−0.867
−1	−1	10.23	590 nm	−0.792
+1	+1	9.65	605 nm	−0.430
+0.5	+1	9.78	600 nm	−0.680
0	+1	9.31	600 nm	−0.629
−0.5	+1	8.04	605 nm	−0.360
−1	+1	7.23	570 nm	−0.331

Table S11 gives the peak full-sphere fourfold visibility and the associated complex phase change.

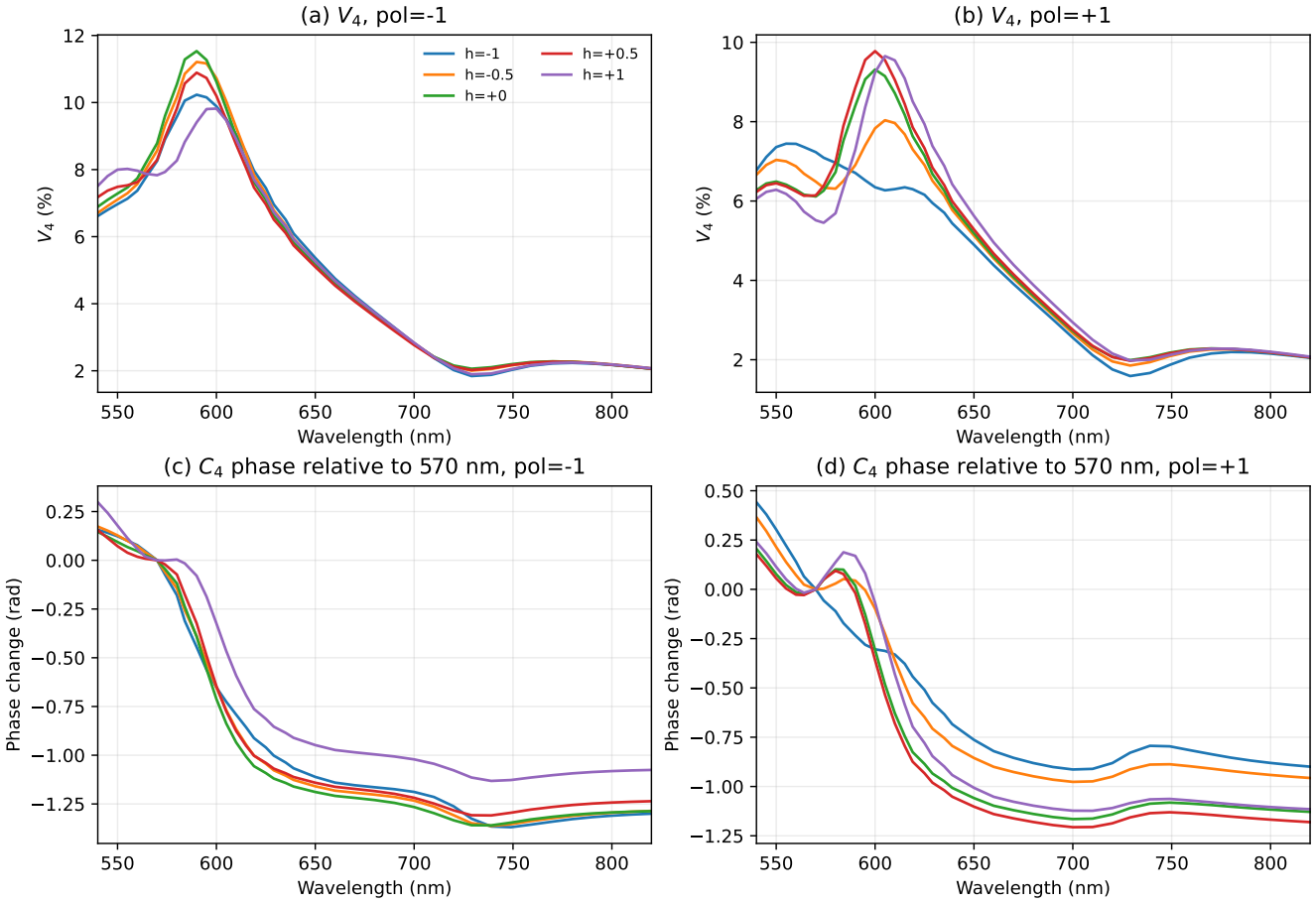


Figure S7: Full-sphere fourfold visibility and complex phase. The strongest visibility and phase rotation occur in the same short-wave band as the maximum secondary electric-octupole weight.

Figure S7 displays the corresponding full-sphere fourfold visibility and phase trajectories.

The strongest case is $h = 0$ under LCP illumination, where $V_4 = 11.53\%$ at 590 nm and $\arg C_4$ changes by -0.935 rad from 570 to 610 nm. This supplies a full-sphere, phase-sensitive Fano indicator independent of the single-direction Argand analysis.

S12 Linear mesh and wavelength convergence

The convergence calculations use the $h = 0$ geometry because it has the strongest full-sphere Fano visibility for LCP. The production physics-controlled Normal mesh and a physics-controlled Fine mesh are compared with all physics, material, boundary, and solver settings unchanged. Across 570–595 nm and both polarizations, the largest Normal-to-Fine differences are 0.326% for scattering, 0.099% for absorption, and 0.127% for extinction.

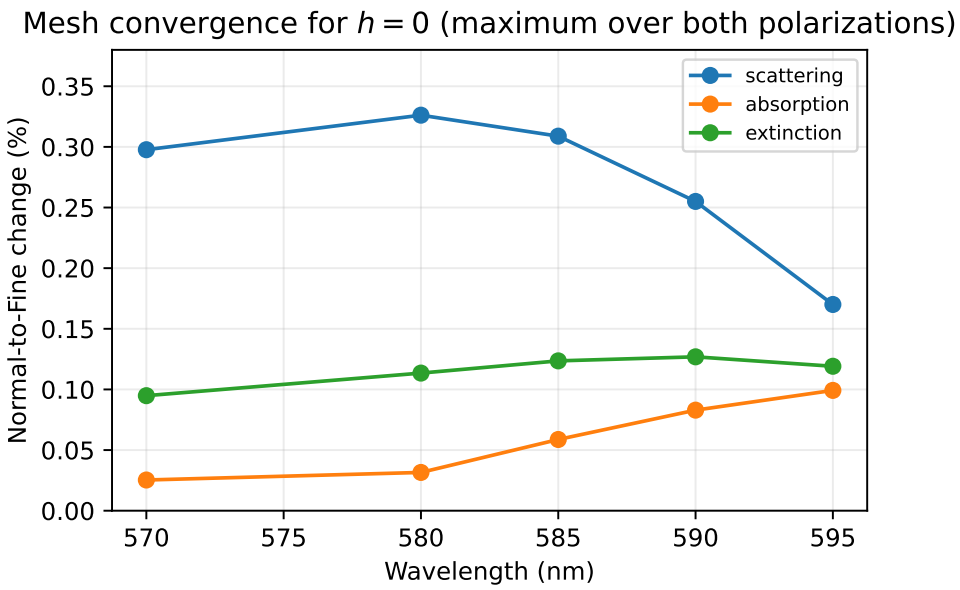


Figure S8: Linear mesh-convergence check for $h = 0$. Curves show the maximum Normal-to-Fine relative change over LCP and RCP at each tested wavelength.

Figure S8 shows the Normal-to-Fine linear mesh-convergence test.

The phase- and multipole-resolved observables are equally stable. At 590 nm under LCP illumination, V_4 changes from 11.5336% to 11.5174%, the total $m = +3$ secondary fraction from 1.2682% to 1.2693%, and the specific $E, \ell = 3, m = +3$ fraction from 1.1790% to 1.1799%. At the broad 730-nm state, the Normal-to-Fine electric-dipole/electric-quadrupole fractions change from 57.97/41.54% to 58.39/41.12% for LCP and from 58.36/41.24% to 58.77/40.83% for RCP; the magnetic-dipole fraction remains below 0.4%.

A separate 1-nm sweep over 575–605 nm resolves the structured feature without changing its interpretation. Quadratic interpolation of the sampled maxima gives, for LCP, $\lambda_{V_4} = 589.86$ nm, $\lambda_{m=+3} = 591.17$ nm, and $\lambda_{E3,+3} = 591.40$ nm. For RCP the corresponding values are 600.06, 599.99, and 600.31 nm. The dense scalar scattering minimum occurs at approximately 590.6 nm for LCP and 596.3 nm for RCP.

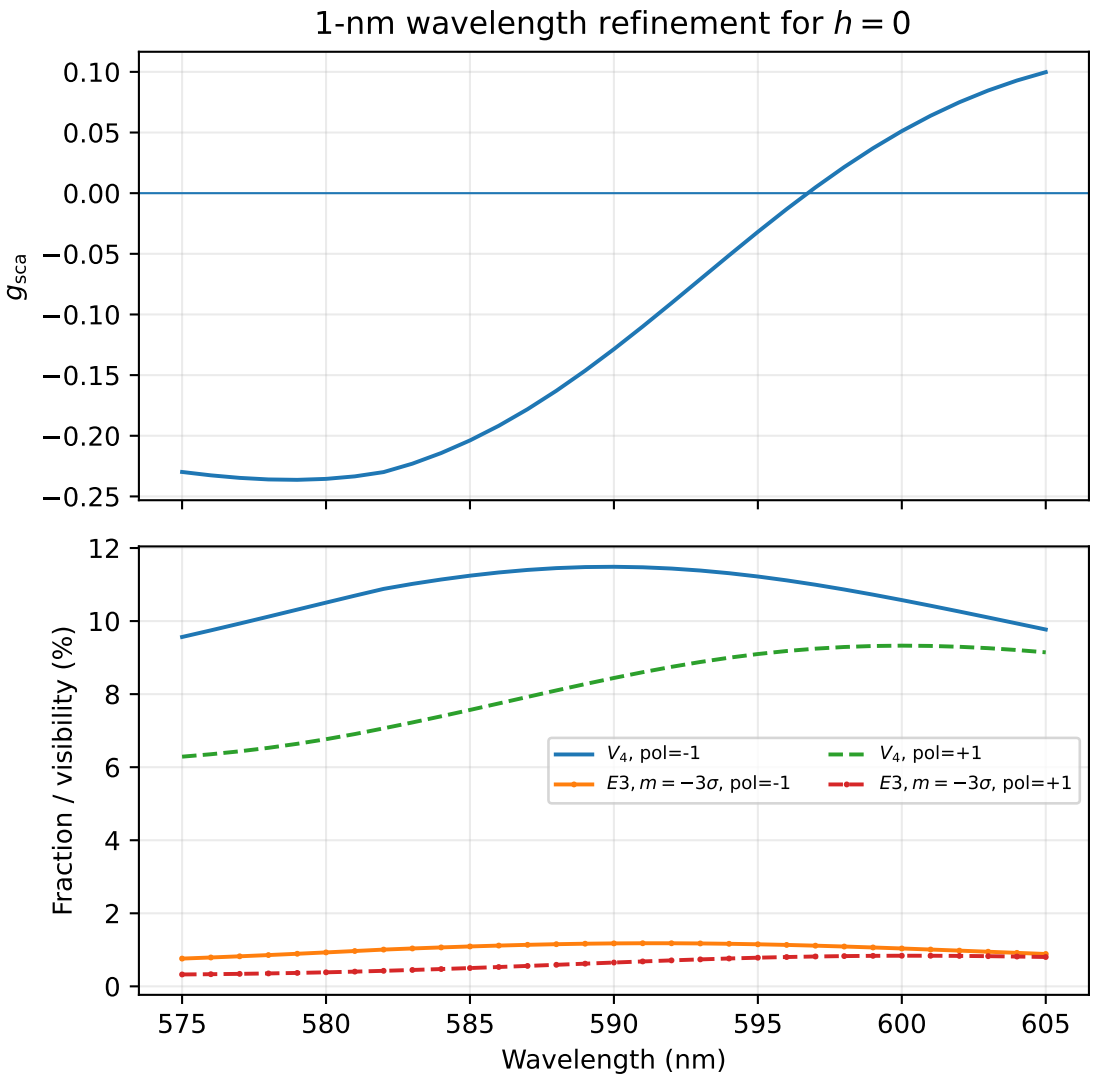


Figure S9: One-nanometer wavelength refinement for $h = 0$. Top: scattering dissymmetry. Bottom: full-sphere fourfold visibility and specific electric-octupole fraction for LCP and RCP.

Figure S9 shows the independent 1-nm spectral refinement of the structured band.

S13 Induced-current phase and overlap diagnostics

The equivalent induced current is

$$\boldsymbol{J}_{\mathrm{ind}} = \mathrm{i}\omega\epsilon_0(\epsilon_{\mathrm{Au}} - \epsilon_h)\boldsymbol{E}, \tag{S37}$$

with $\epsilon_h = 1.69$. The current is evaluated on the fixed $z = 50$ nm cut plane for $h = 0$ under LCP illumination. The main manuscript shows the common-scale 580/590/600/730-nm current array. The supplementary phase-quadrature view below instead normalizes the magnitude within each wavelength so that the real and 90°-shifted current topology can be compared without the larger 730-nm amplitude dominating the display.

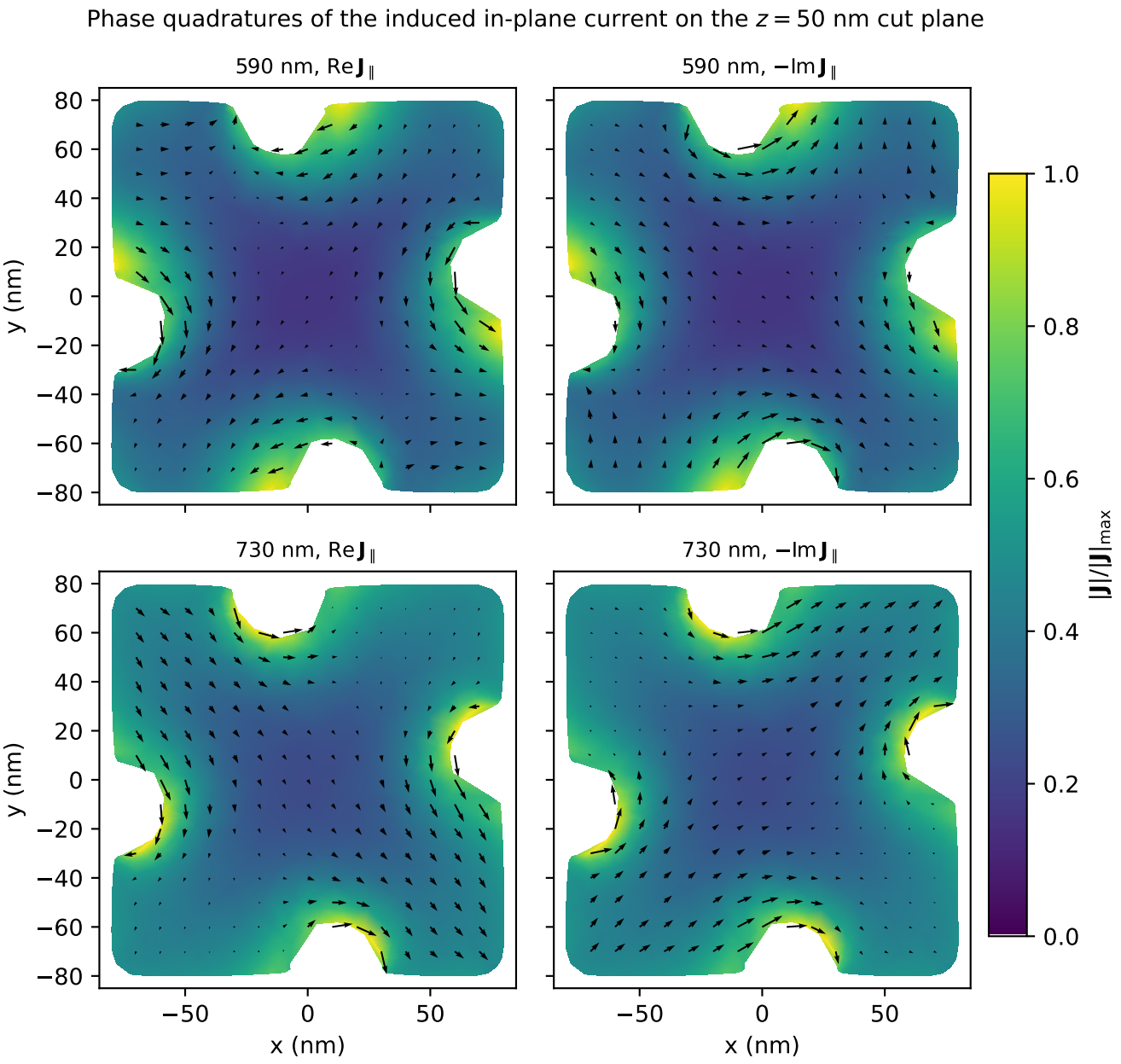


Figure S10: Normalized phase quadratures of the in-plane induced current at 590 and 730 nm on the same $z = 50$ nm plane. Arrows show Re $\boldsymbol{J}_\parallel$ and $-$Im $\boldsymbol{J}_\parallel$; each wavelength is normalized for topology visualization only.

Figure S10 compares the induced-current phase quadratures in the structured and broad spectral states.

For quantitative comparison the complex fields are interpolated to a common 1-nm Cartesian grid and integrated only over the common valid gold region. The normalized overlap

$$C_J = \frac{\int \boldsymbol{J}_1^* \cdot \boldsymbol{J}_2 \, dA}{\sqrt{\int |\boldsymbol{J}_1|^2 dA \int |\boldsymbol{J}_2|^2 dA}} \tag{S38}$$

gives the values in table S12.

On the same common grid, the fraction of $\int |\boldsymbol{J}|^2 dA$ carried by J_z decreases from 45.2% at 580 nm to 42.5% at 590 nm, 41.5% at 600 nm, and 33.2% at 730 nm. The integrated cut-plane current intensity at 730 nm is about 12.9 times its 590-nm value. This ratio is a local driven-current diagnostic, not a substitute for the total radiated power.

Table S12: Complex induced-current overlap on the common $z = 50$ nm cut plane.

Pair (nm)	$\lvert C_J \rvert$	$\arg C_J$	$\sqrt{1 - \lvert C_J \rvert^2}$
580–590	0.9907	6.61°	0.136
590–600	0.9937	6.52°	0.112
580–600	0.9705	12.82°	0.241
580–730	0.7650	58.33°	0.644
590–730	0.8223	55.18°	0.569
600–730	0.8705	50.34°	0.492

S14 Finite collection-angle observables

For a cone about $\pm z$, the collected dissymmetry and mean collection efficiency are defined as in the main manuscript. Calculations were performed for $\theta_c = 15°, 30°, 45°, 60°, 90°$, corresponding in the homogeneous $n_h = 1.3$ host to NA= 0.34, 0.65, 0.92, 1.13, 1.30. The main manuscript shows all-h spectra at $\theta_c = 30°$; here we retain only the collection-angle tradeoff.

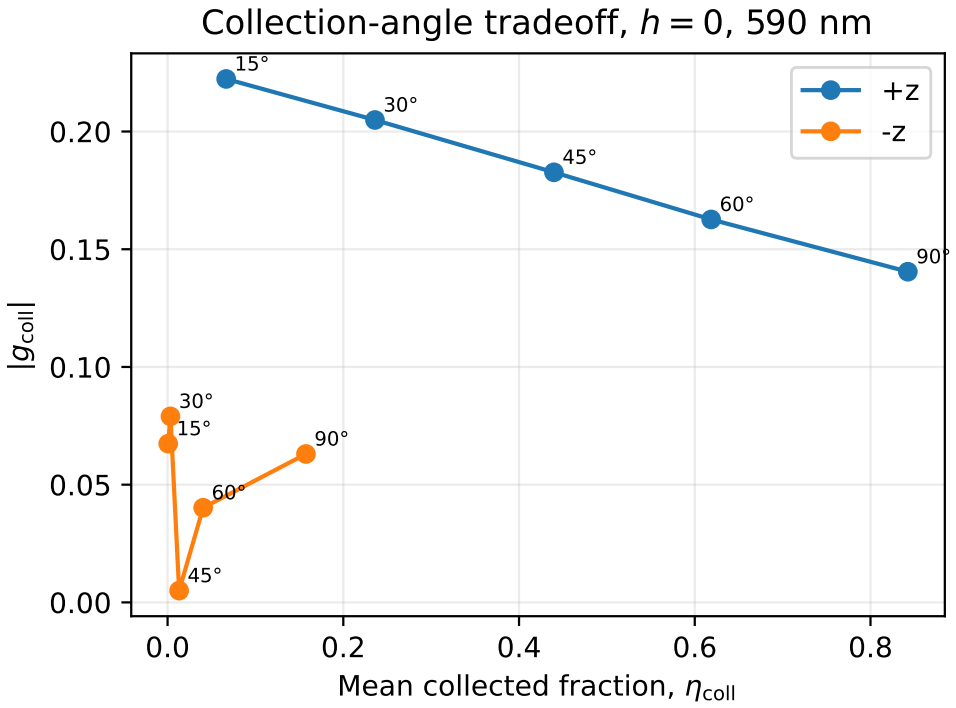


Figure S11: Tradeoff between collected dissymmetry magnitude and mean collected fraction for $h = 0$ at 590 nm as the cone half-angle is increased. Labels give θ_c. Large directional $|g|$ in the $-z$ cone occurs at very low collected power.

Figure S11 shows how directional dissymmetry trades against collected radiated power.

At $h = 0$, 590 nm, the $+z$ 30° cone gives $g_{\mathrm{coll}} = -0.205$ and $\eta_{\mathrm{coll}} = 0.236$, compared with $g_{\mathrm{sphere}} = -0.128$. The corresponding $-z$ cone gives $g_{\mathrm{coll}} = +0.079$ but only $\eta_{\mathrm{coll}} = 0.00328$. Across all geometries at 30°, the largest useful $+z$ enhancement occurs for $h = -0.5$, 580 nm, with $g_{\mathrm{coll}} = -0.384$ and $\eta_{\mathrm{coll}} = 0.250$. The largest absolute $-z$ value is +0.303 for $h = -1$ near 585 nm, but its mean collected fraction is only 4.74×10^{-4}.

S15 Damped-oscillator and Fano derivation

The derivation follows the configuration-interaction picture of Fano interference and its plasmonic and temporal coupled-mode implementations [4], [5], [6], [7], [8].

S15.1 One oscillator

A driven coordinate obeys

$$\ddot{x} + \gamma\dot{x} + \omega_0^2 x = Fe^{-\mathrm{i}\omega t}. \tag{S39}$$

With $x = \widetilde{x}e^{-\mathrm{i}\omega t}$,

$$\widetilde{x} = \frac{F}{\omega_0^2 - \omega^2 - \mathrm{i}\gamma\omega}. \tag{S40}$$

Near resonance,

$$\omega_0^2 - \omega^2 - \mathrm{i}\gamma\omega \simeq 2\omega_0\left(\omega_0 - \omega - \mathrm{i}\frac{\gamma}{2}\right), \tag{S41}$$

which yields the first-order complex pole used in coupled-mode theory.

S15.2 Two coupled oscillators

For broad and narrower coordinates,

$$D_b^{(2)} x_b + G x_d = F_b, \tag{S42}$$

$$G x_b + D_d^{(2)} x_d = F_d, \tag{S43}$$

where $D_j^{(2)} = \omega_j^2 - \omega^2 - \mathrm{i}\gamma_j\omega$. The exact broad response is

$$x_b = \frac{F_b D_d^{(2)} - G F_d}{D_b^{(2)} D_d^{(2)} - G^2}. \tag{S44}$$

After near-resonance reduction,

$$a_b = \frac{f_b D_d - \kappa f_d}{D_b D_d - \kappa^2}, \qquad a_d = \frac{f_d D_b - \kappa f_b}{D_b D_d - \kappa^2}. \tag{S45}$$

If $f_d = 0$,

$$a_b = \frac{f_b}{D_b - \kappa^2/D_d}, \qquad a_d = -\frac{\kappa}{D_d} a_b. \tag{S46}$$

The poles are zeros of $D_b D_d - \kappa^2$. A measured radiative amplitude,

$$A = c_{\mathrm{bg}} + c_b a_b + c_d a_d, \tag{S47}$$

can have a zero at a different frequency. The distinction between pole motion and zero motion is the basis of the interpretation used in the main manuscript.

S16 Surface-SHG implementation

S16.1 Implemented surface source

For centrosymmetric gold, the present model retains an effective tangential surface term

$$\boldsymbol{P}_s^{(2)}(2\omega) = \epsilon_0 \chi_{tnt}^{(2)} E_n \boldsymbol{E}_t, \tag{S48}$$

where $E_n = \boldsymbol{n} \cdot \boldsymbol{E}_\omega$ and $\boldsymbol{E}_t = \boldsymbol{E}_\omega - E_n \boldsymbol{n}$ are evaluated on the gold side of the interface. This is a fixed effective model input; the work does not extract absolute nonlinear susceptibility coefficients. Surface-SHG descriptions of centrosymmetric noble metals commonly use normal/tangential surface-field combinations [2].

The pump-side Cartesian definitions used before retrieval are:

```
ExAu = if(up(dom)==3,up(ewfd.Ex),down(ewfd.Ex))
EyAu = if(up(dom)==3,up(ewfd.Ey),down(ewfd.Ey))
EzAu = if(up(dom)==3,up(ewfd.Ez),down(ewfd.Ez))
```

```
nAux = if(up(dom)==3,unx,dnx)
nAuy = if(up(dom)==3,uny,dny)
nAuz = if(up(dom)==3,unz,dnz)

En_p = nAux*ExAu+nAuy*EyAu+nAuz*EzAu
Etx_p = ExAu-En_p*nAux
Ety_p = EyAu-En_p*nAuy
Etz_p = EzAu-En_p*nAuz

Psx = epsilon0_const*chi2s*En_p*Etx_p
Psy = epsilon0_const*chi2s*En_p*Ety_p
Psz = epsilon0_const*chi2s*En_p*Etz_p
```

S16.2 Direct indexed retrieval of the stored pump source

Each pump-source component is retrieved directly from the stored pump solution with an explicit wavelength index and polarization value. Schematically,

```
Psx_SH = withsol('sol2',Psx,
 setind(lambda0,pump_i),setval(pol,-1))
Psy_SH = withsol('sol2',Psy,
 setind(lambda0,pump_i),setval(pol,-1))
Psz_SH = withsol('sol2',Psz,
 setind(lambda0,pump_i),setval(pol,-1))
```

for the minus branch, with `setval(pol,1)` for the plus branch. The manual index obeys

$$\lambda_0 = 1080\ \text{nm} + (\texttt{pump_i} - 1)10\ \text{nm}. \tag{S49}$$

The source–field overlap expression is

```
ovSH_SH = conj(ewfd2.Ex)*Psx_SH
 + conj(ewfd2.Ey)*Psy_SH
 + conj(ewfd2.Ez)*Psz_SH
```

The same retrieved source components are used both to drive the SH field and to evaluate this diagnostic.

Representative direct comparisons of pump pointwise products and their `withsol()` retrieval agree at the percent level or better. This check is more discriminating than comparing only integrated pump quantities because the SH source depends on local products such as $E_n \boldsymbol{E}_t$.

S16.3 Radiated SH power and closure

The radiated power is evaluated from the solved 2ω field,

$$P_{2\omega} = \int_{S_{\text{FF}}} \texttt{ewfd2.nPoav}\, dS. \tag{S50}$$

Upper- and lower-surface partitions are retained as a diagnostic. The power partitions satisfy

$$P_{\text{total}} = P_{\text{up}} + P_{\text{down}} \tag{S51}$$

to numerical precision, which is used as a bookkeeping check.

S17 Five-state nonlinear spectra: numerical record

The wavelength-resolved nonlinear spectra, their extrema, and the polarization-averaged SH powers are shown in the main manuscript and are not duplicated here. This section instead identifies the machine-readable numerical

record underlying those main-text results. The files `data/shg_spectrum_h_p1.csv`, `shg_spectrum_h_p0p5.csv`, `shg_spectrum_h_0.csv`, `shg_spectrum_h_m0p5.csv`, and `shg_spectrum_h_m1.csv` contain the five complete spectra, while `data/nonlinear_extrema.csv` contains the extrema quoted in the main text.

The 600-nm trajectory is monotonic in h, but the complete spectra are not monotonic in every spectral interval. Large $|g_{\mathrm{SHG}}|$ values must therefore be interpreted together with the corresponding mean radiated power. The mechanistic quantities that are genuinely supplementary, including the focused nonlinear mesh test and the source–overlap–radiation hierarchy, begin in Secs. S18 and S19.

S18 Focused nonlinear mesh convergence

A dedicated end-to-end mesh-refinement check was performed for the strongest positive nonlinear-dissymmetry point, $h = -1$ at $\lambda_{2\omega} = 600$ nm. Unlike a refinement of the SH solve alone, the Fine-mesh test recomputes both pump polarizations at $\lambda_\omega = 1200$ nm and then uses those Fine-mesh pump fields to construct and radiate the corresponding surface nonlinear sources at 600 nm. The source definition, material model, boundary conditions, and SH-power evaluation are otherwise unchanged.

Table S13: Focused nonlinear Normal-to-Fine mesh convergence for $h = -1$ at $\lambda_\omega = 1200$ nm ($\lambda_{2\omega} = 600$ nm). The minus numerical polarization is LCP and the plus numerical polarization is RCP under the convention of the main manuscript.

Mesh	$P_{2\omega}^{\mathrm{LCP}}$	$P_{2\omega}^{\mathrm{RCP}}$	g_{SHG}
Normal	4.2291×10^{-29}	1.4365×10^{-29}	0.9858
Fine	4.1990×10^{-29}	1.4414×10^{-29}	0.9778

Table S13 reports the end-to-end nonlinear Normal-to-Fine convergence values.

The Fine mesh changes the LCP and RCP SH powers by -0.71% and $+0.34\%$, respectively. The dissymmetry changes by only $\Delta g_{\mathrm{SHG}} = -0.0080$ (0.81% relative), from 0.9858 to 0.9778. Thus both absolute SH powers and the near-unity polarization contrast are stable under the focused end-to-end refinement. This calculation validates the principal nonlinear headline point; it is not intended as an exhaustive Fine-mesh sweep over all five geometries and all pump wavelengths.

S19 Source, overlap, and radiation diagnostics

S19.1 Definitions

The full-surface nonlinear-source norm is

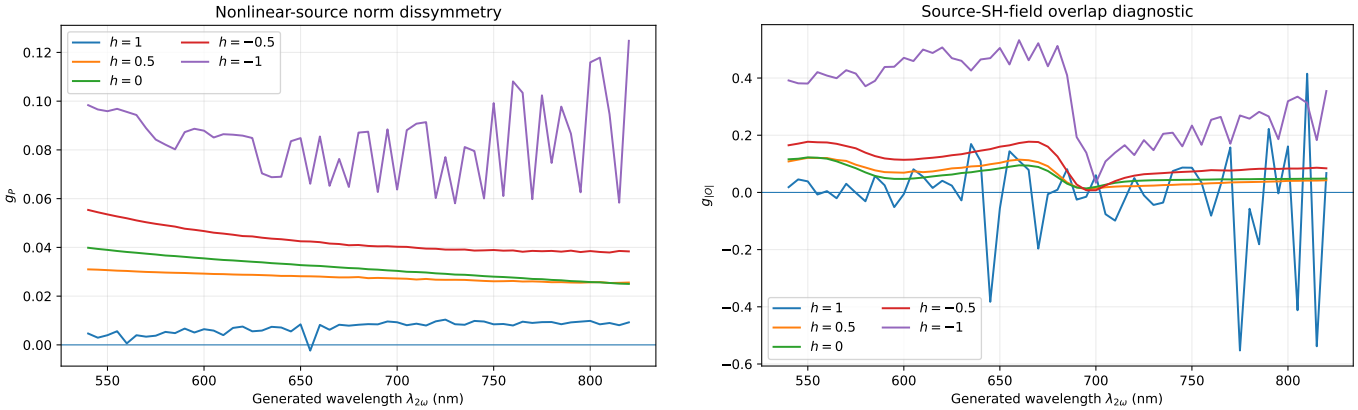
$$S_P^{(s)} = \int_{S_{\mathrm{Au}}} \left(|P_{sx,\mathrm{SH}}^{(s)}|^2 + |P_{sy,\mathrm{SH}}^{(s)}|^2 + |P_{sz,\mathrm{SH}}^{(s)}|^2 \right) dS. \tag{S52}$$

It is a squared source norm, not an incident power, SH power, or conversion efficiency. It discards relative phase between different surface regions.

The source–field overlap is

$$O_{\mathrm{SH}}^{(s)} = \int_{S_{\mathrm{Au}}} \boldsymbol{E}_{2\omega}^{(s)*} \cdot \boldsymbol{P}_{s,\mathrm{SH}}^{(2,s)} \, dS. \tag{S53}$$

We report a magnitude dissymmetry $g_{|O|}$ only as a response diagnostic. Because $\boldsymbol{E}_{2\omega}$ is generated by the same source, O_{SH} is not an independent eigenmode-overlap coefficient.



(a) Source-norm dissymmetry.

(b) Overlap-magnitude dissymmetry.

Figure S12: Source-level diagnostics over the complete nonlinear sweep. Neither scalar source norm nor overlap magnitude alone reproduces the final radiated g_{SHG}.

Figure S12 compares the source-norm and source–field-overlap dissymmetries across the complete nonlinear sweep.

S19.2 Six-hundred-nanometer hierarchy

At a generated wavelength of 600 nm the three levels separate cleanly:

Table S14: Source, overlap, and radiated-SH diagnostics at 600 nm.

h	g_P	$g_{\lvert O\rvert}$	g_{SHG}	$S_{P,\mathrm{LCP}}/S_{P,\mathrm{RCP}}$	$P_{\mathrm{LCP}}/P_{\mathrm{RCP}}$	$\mathcal{R}_{\mathrm{LCP}}/\mathcal{R}_{\mathrm{RCP}}$
+1	0.006439	−0.005802	−0.130545	1.006459	0.877454	0.871823
+0.5	0.029233	0.068989	0.156537	1.029667	1.169829	1.136123
0	0.035492	0.047232	0.326871	1.036133	1.390731	1.342231
−0.5	0.046690	0.114078	0.572755	1.047806	1.802603	1.720360
−1	0.087882	0.470725	0.985815	1.091921	2.944052	2.696213

Table S14 gives the numerical source, overlap, and radiated-power hierarchy at 600 nm.

Here

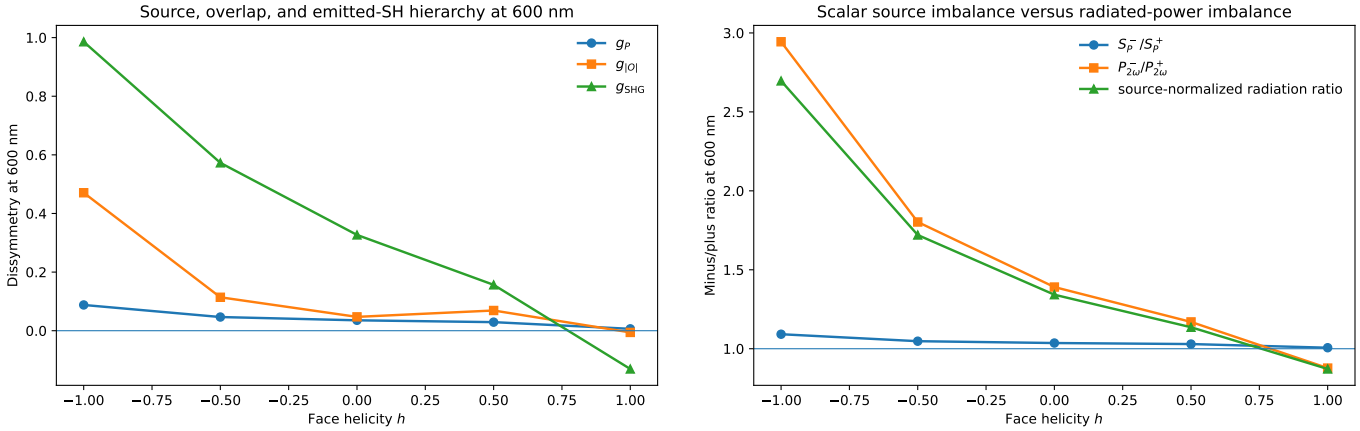
$$\frac{\mathcal{R}_{\mathrm{LCP}}}{\mathcal{R}_{\mathrm{RCP}}} = \frac{P_{\mathrm{LCP}}/P_{\mathrm{RCP}}}{S_{P,\mathrm{LCP}}/S_{P,\mathrm{RCP}}} \tag{S54}$$

is only a source-normalized radiation diagnostic. It is not a material efficiency or an independent physical factorization of the nonlinear process.

For $h = -1$, an approximately 9.2% source-norm imbalance becomes a nearly 3:1 radiated-power imbalance. The residual factor is

$$\frac{2.944052}{1.091921} = 2.696213 \simeq 2.70. \tag{S55}$$

Thus scalar source magnitude alone cannot explain the radiated LCP/RCP contrast.



(a) Dissymmetry hierarchy.

(b) LCP/RCP ratios.

Figure S13: Source generation and radiated SH response at 600 nm.

Figure S13 visualizes the same hierarchy and the associated LCP/RCP ratios.

S19.3 A stronger sign test at $h = -1$, 550 nm

At the short-wave minimum of the $h = -1$ geometry, where the selected face is right-handed while the remaining helicoid is left-handed,

$$g_P = +0.095876, \qquad g_{|O|} = +0.380674, \qquad g_{\mathrm{SHG}} = -0.934255. \tag{S56}$$

The radiated dissymmetry therefore has the *opposite sign* from both the scalar source norm and overlap magnitude. This is a stronger counterexample to a scalar-source explanation than the 600-nm magnitude comparison alone. It demonstrates that the complex vector/spatial structure of the source and its electromagnetic propagation at 2ω are indispensable.

S20 Pump-field localization retained only as a pump diagnostic

The signed-normal-field diagnostic is retained as a pump-only visualization (Figure S14). It uses only the stored fundamental solution and is not used as the principal explanation of the SHG dissymmetry.

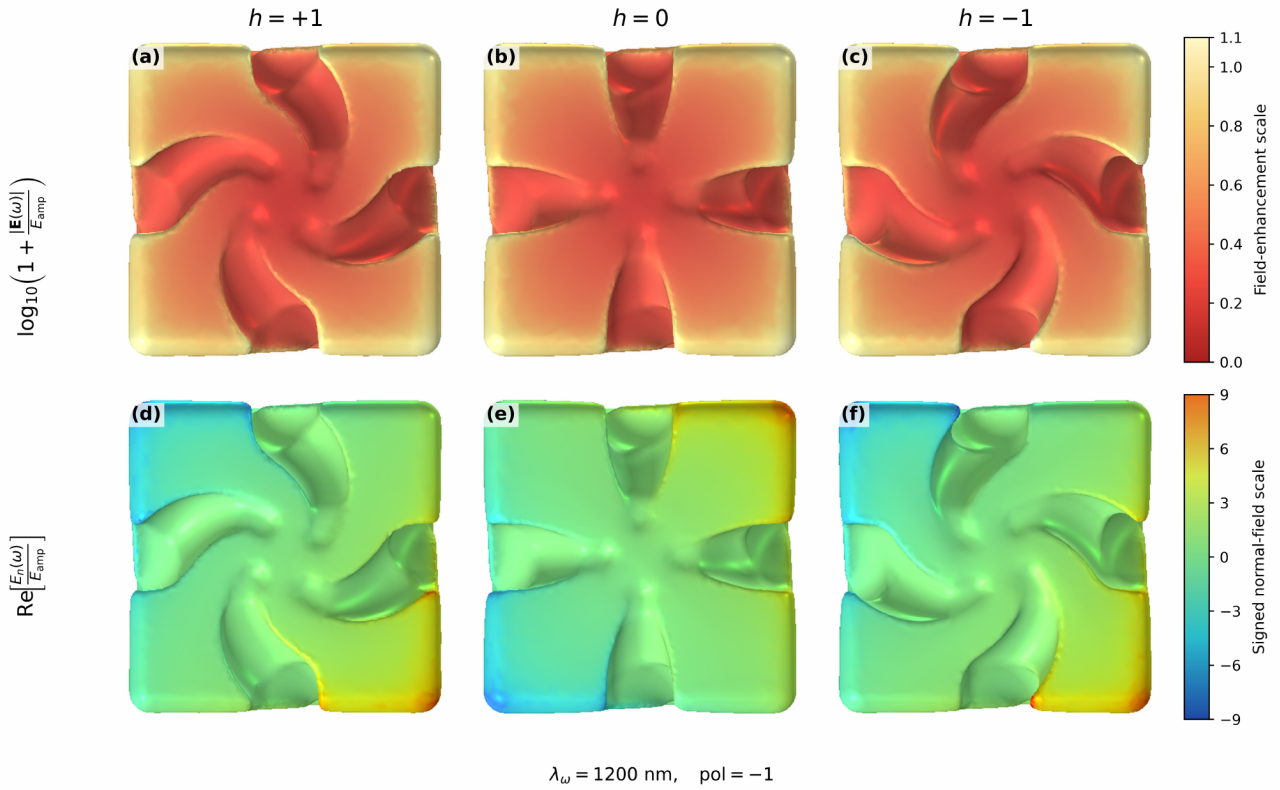


Figure S14: Face-on magnitude and signed-normal-field diagnostics at $\lambda_\omega = 1200$ nm for LCP. The signed row retains phase information absent from $|E|$ and shows that the local normal-field organization changes with selected-face winding.

The $|E_\omega|^2$ and $|E_\omega|^4$ localization calculations at $\lambda_\omega = 1200$ nm depend only on the stored pump solution and remain valid as pump-only diagnostics. They are *not* used as the main nonlinear mechanism evidence in the nonlinear interpretation.

For the modified face S_f and total gold surface S_{Au},

$$Q_{n,f} = \int_{S_f} |E_\omega|^n dS, \qquad Q_{n,\mathrm{all}} = \int_{S_{\mathrm{Au}}} |E_\omega|^n dS, \tag{S57}$$

with localization fraction $L_n = Q_{n,f}/Q_{n,\mathrm{all}}$ and face/background concentration ratio

$$C_n = \frac{Q_{n,f}/A_f}{(Q_{n,\mathrm{all}} - Q_{n,f})/(A_{\mathrm{all}} - A_f)}. \tag{S58}$$

Table S15: Pump-only localization metrics at $\lambda_\omega = 1200$ nm. Columns + and − denote RCP and LCP, respectively.

		L_2		C_2		L_4		C_4		
h	A_f/A_{all}	+	−	+	−	+	−	+	−	$g_{Q_4,f}$
+1	0.1668	0.1410	0.1453	0.8198	0.8491	0.1483	0.1483	0.8698	0.8696	0.0122
+0.5	0.1648	0.1405	0.1442	0.8282	0.8541	0.1452	0.1492	0.8607	0.8884	0.0484
0	0.1637	0.1406	0.1439	0.8360	0.8587	0.1395	0.1460	0.8286	0.8731	0.0764
−0.5	0.1653	0.1444	0.1470	0.8521	0.8705	0.1509	0.1710	0.8975	1.0420	0.2055
−1	0.1637	0.1431	0.1465	0.8531	0.8766	0.1454	0.1583	0.8692	0.9607	0.1342

Table S15 shows that pump localization changes more modestly than the SHG trajectory. They are used only as pump-field diagnostics; the nonlinear mechanism is evaluated from the full-surface source norm, source–field overlap, and radiated SH power defined above.

S21 Spectral connection between linear Fano interference and SHG

The linear phase-sensitive output minima lie at 585–595 nm for LCP and RCP across all five geometries. The strongest nonlinear $|g_{\mathrm{SHG}}|$ feature within 580–615 nm occurs at:

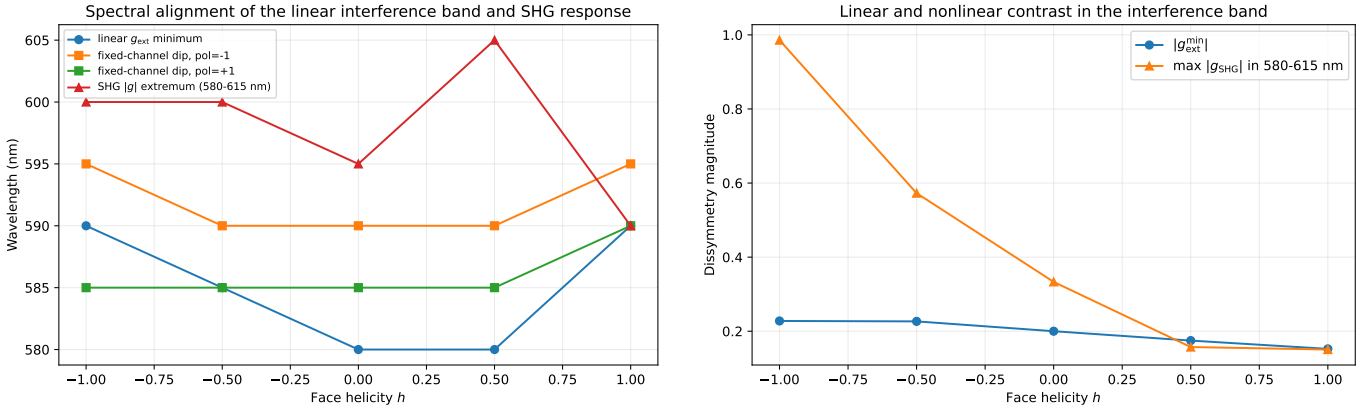
$$590,\ 605,\ 595,\ 600,\ 600 \text{ nm} \tag{S59}$$

for $h = +1, +0.5, 0, -0.5, -1$, respectively. Thus face reversal changes the *magnitude and sign* of the nonlinear contrast far more strongly than it moves the generated-frequency spectral feature.

Table S16: Linear Fano landmarks compared with the nonlinear feature.

h	fixed-channel dip, LCP	fixed-channel dip, RCP	linear g_{ext} minimum	SH band extremum
+1	595 nm	590 nm	−0.15233 at 590 nm	−0.15057 at 590 nm
+0.5	590 nm	585 nm	−0.17475 at 580 nm	+0.15727 at 605 nm
0	590 nm	585 nm	−0.20003 at 580 nm	+0.33314 at 595 nm
−0.5	590 nm	585 nm	−0.22657 at 585 nm	+0.57276 at 600 nm
−1	595 nm	585 nm	−0.22769 at 590 nm	+0.98582 at 600 nm

Table S16 compares the spectral landmarks. The magnitude of the scalar linear extinction dissymmetry changes only from roughly 0.15 to 0.23, whereas the nonlinear band contrast grows to nearly unity. The ratio of the nonlinear band-extremum magnitude to the linear scalar-extinction-extremum magnitude is approximately 0.99, 0.90, 1.67, 2.53, and 4.33 from $h = +1$ to $h = -1$.



(a) Spectral alignment.

(b) Contrast magnitude.

Figure S15: The nonlinear feature remains in the independently established visible-frequency Fano band while its dissymmetry grows much more strongly than the scalar linear response.

Figure S15 visualizes the spectral alignment and contrast growth. This comparison does *not* mean that linear CD is simply amplified by SHG. Indeed, the nonlinear sign reverses along the h trajectory while the scalar linear extinction minimum remains negative. The defensible statement is instead that face helicity reweights the complex coupling of the nonlinear surface source to a phase-sensitive radiation problem at 2ω inside an essentially fixed interference band. Because $\lambda_{2\omega} = 600$ nm corresponds to a pump wavelength of 1200 nm, the spectral coincidence specifically points to the generated-frequency electromagnetic response rather than a pump resonance at 600 nm.

S22 Heuristic nonlinear coupled-mode extension

The following reduced model is retained only to show where coherent nonlinear interference can enter; it is not fitted to the SH data and is not used to claim a unique nonlinear Fano eigenmode. If hypothetical pump amplitudes are a_b and a_d, a projected nonlinear source may contain

$$S_s^{(2)} = \beta_{b,s} a_{b,s}^2 + \beta_{d,s} a_{d,s}^2 + 2\beta_{bd,s} a_{b,s} a_{d,s}. \tag{S60}$$

Using $a_d = -(\kappa/D_d)a_b$ gives

$$S_s^{(2)} = a_{b,s}^2 \left[\beta_{b,s} - 2\beta_{bd,s} \frac{\kappa_s}{D_{d,s}} + \beta_{d,s} \left(\frac{\kappa_s}{D_{d,s}} \right)^2 \right]. \tag{S61}$$

The bracket can contain a complex zero. A separate converted-frequency response can introduce additional resonant and interference structure. The simulations do not uniquely separate source-phase interference from propagation through the 2ω Green operator, so this model remains conceptual. This is consistent with the broader observation that Fano interference can disproportionately alter nonlinear output relative to a scalar drive amplitude [8].

S23 Nonlinear numerical workflow

The nonlinear calculation is reproduced by the following sequence:

1. solve the pump interface for all λ_ω = 1080–1640 nm and both circular inputs, LCP and RCP;
2. define the gold-side normal and tangential pump fields and the pump-side source components `Psx`, `Psy`, and `Psz`;
3. retrieve each source component in the SH model with `withsol('sol2',...setind(lambda0,pump_i),setval(pol,s))`;
4. use the retrieved `Ps*_SH` components to drive the 2ω source;
5. evaluate P_{total}, P_{up}, and P_{down} from `ewfd2.nPoav` and verify $P_{\text{total}} = P_{\text{up}} + P_{\text{down}}$;
6. evaluate S_P from the same `Ps*_SH` source components;
7. evaluate `ovSH_SH` from the same source components when the source–field overlap diagnostic is required;
8. form each dissymmetry factor only after the two polarization-resolved scalar quantities have been obtained.

S24 Radiation-channel and reproducibility scope

Table S17 summarizes the numerical records used throughout this work. The full-sphere analysis maps the equatorial Fourier indices onto spherical radiation multipoles: the weak $m = -3\sigma$ family is predominantly electric $\ell = 3$, while the dominant $m = \sigma$ family contains substantial electric-dipole, electric-quadrupole, and magnetic-dipole radiation. This resolves the radiated multipolar content but does not create a one-to-one map to open-system eigenmodes. The main-text claims are therefore restricted to radiation and driven-current channels.

Table S17: Numerical records and reproducibility scope.

Item	Record used in this work
Geometry series	Connected geometries $h = +1, +0.5, 0, -0.5, -1$ with one selected face varied and the remaining structure held fixed.
Linear response	$\sigma_{\text{sca}}^{(\text{LCP/RCP})}$, $\sigma_{\text{abs}}^{(\text{LCP/RCP})}$, and $\sigma_{\text{ext}}^{(\text{LCP/RCP})}$ for all five geometries.
Surface SHG	Pump wavelengths 1080–1640 nm; generated wavelengths 540–820 nm; stored pump source retrieved with explicit wavelength and numerical polarization indices.
Nonlinear source	Full-surface $S_P^{(\text{LCP/RCP})}$ from the same retrieved $P_{sx,\text{SH}}, P_{sy,\text{SH}}, P_{sz,\text{SH}}$ components used in the SH solve.
Source–field diagnostic	$O_{\text{SH}}^{(\text{LCP/RCP})} = \int \boldsymbol{E}_{2\omega}^* \cdot \boldsymbol{P}_s^{(2)} dS$, evaluated with the same retrieved source.
Radiated SH	P_{total}, P_{up}, and P_{down} from `ewfd2.nPoav`; the partition closure $P_{\text{total}} = P_{\text{up}} + P_{\text{down}}$ is verified numerically.
Gold dispersion	Johnson–Christy optical data [1] as implemented in the COMSOL gold material at pump and generated frequencies.
Equatorial complex far field	Complex Cartesian far-field components, azimuth, wavelength, and circular-polarization label on the fixed circle.
Full-sphere complex far field	Complex Cartesian fields, θ, ϕ, wavelength, and circular-polarization index for all five geometries.
Full-sphere analysis	VSH analysis through $\ell_{\max} = 8$ and finite-collection observables for five cone angles about $\pm z$.
Driven current	Common $z = 50$ nm cut-plane analysis at 580, 590, 600, and 730 nm for $h = 0$ under LCP illumination.
Linear convergence	Normal-to-Fine mesh comparison in the structured band and at the broad state, plus 1-nm wavelength refinement from 575 to 605 nm.

Table S17 (continued)

Item	Record used in this work
Nonlinear convergence	End-to-end Normal-to-Fine check for $h = -1$ at a 1200-nm pump / 600-nm generated wavelength, recomputing both pump polarizations and both SH outputs on the Fine mesh.
Polarization labels	LCP/RCP labels and the dissymmetry sign follow the convention defined once in the main manuscript; numerical `pol` values are retained only in COMSOL/data-retrieval expressions.

S25 Data products in this package

Online Resource 1 contains the supplementary figures and diagnostics. Online Resource 2 contains 34 analysis-ready numerical tables in its `data/` directory and a file inventory. Large raw COMSOL field exports are not duplicated. The nonlinear tables include the five g_{SHG} spectra, the 600-nm hierarchy, the nonlinear extrema, and the linear-Fano/SHG spectral comparison used in the manuscript and this Supplementary Information.

S26 Summary

The short-wave 560–610 nm linear response is a converged, phase-sensitive, low-rank radiation-interference problem. Fixed-channel minima near 585–595 nm coincide with rapid phase rotations; the equatorial field is dominated by $m = \sigma$ and $m = -3\sigma$; the latter is predominantly electric-octupolar on the full sphere; and mesh/wavelength refinement leaves the assignment intact. The broad response near 730 nm remains a distinct ED/EQ-dominated state.

Direct indexed retrieval of the stored pump-derived surface source gives

$$g_{\mathrm{SHG}}(600\ \mathrm{nm}) = (-0.1305,\ +0.1565,\ +0.3269,\ +0.5728,\ +0.9858)$$

for $h = (+1, +0.5, 0, -0.5, -1)$. A focused end-to-end Fine-mesh recalculation of the headline $h = -1$ point changes the LCP/RCP SH powers from $4.2291 \times 10^{-29}/1.4365 \times 10^{-29}$ to $4.1990 \times 10^{-29}/1.4414 \times 10^{-29}$ and changes g_{SHG} only from 0.9858 to 0.9778. Over the same five-state trajectory the scalar source-norm dissymmetry grows only from 0.0064 to 0.0879. At $h = -1$, a source ratio of 1.0919 becomes a radiated-power ratio of 2.9441, giving a source-normalized radiation ratio of 2.696. At 550 nm the $h = -1$ structure, with a right-handed selected face on the otherwise left-handed helicoid, provides an even stronger sign test: positive source and overlap-magnitude dissymmetries accompany a negative radiated $g_{\mathrm{SHG}} = -0.934$, showing that scalar source strength does not determine the output even at the level of sign.

The strongest nonlinear feature remains at 590–605 nm generated wavelength, coincident with the independently established linear Fano-interference band. Face helicity therefore reweights the complex coupling of the nonlinear surface polarization to phase-sensitive radiative channels at 2ω. The data support Fano-enhanced nonlinear chiroptical radiation without requiring a unique nonlinear eigenmode assignment.

References

[1] P. B. Johnson and R. W. Christy, "Optical constants of the noble metals," *Physical Review B*, vol. 6, no. 12, pp. 4370–4379, 1972. DOI: 10.1103/PhysRevB.6.4370

[2] F. Spreyer et al., "Second-harmonic optical circular dichroism of plasmonic chiral helicoid-iii nanoparticles," *ACS Photonics*, vol. 9, no. 3, pp. 784–792, 2022. DOI: 10.1021/acsphotonics.1c00882

[3] P. Grahn, A. Shevchenko, and M. Kaivola, "Electromagnetic multipole theory for optical nanomaterials," *New Journal of Physics*, vol. 14, no. 9, p. 093 033, 2012. DOI: 10.1088/1367-2630/14/9/093033

[4] U. Fano, "Effects of configuration interaction on intensities and phase shifts," *Physical Review*, vol. 124, no. 6, pp. 1866–1878, 1961. DOI: 10.1103/PhysRev.124.1866

[5] B. Lukyanchuk et al., "The fano resonance in plasmonic nanostructures and metamaterials," *Nature Materials*, vol. 9, pp. 707–715, 2010. DOI: 10.1038/nmat2810

[6] S. Fan, W. Suh, and J. D. Joannopoulos, "Temporal coupled-mode theory for the fano resonance in optical resonators," *Journal of the Optical Society of America A*, vol. 20, no. 3, pp. 569–572, 2003. DOI: 10.1364/JOSAA.20.000569

[7] W. Suh, Z. Wang, and S. Fan, "Temporal coupled-mode theory and the presence of non-orthogonal modes in lossless multimode cavities," *IEEE Journal of Quantum Electronics*, vol. 40, no. 10, pp. 1511–1518, 2004. DOI: 10.1109/JQE.2004.834773

[8] D. Turkpence, G. B. Akguc, A. Bek, and M. E. Tasgin, "Engineering nonlinear response of nanomaterials using fano resonances," *Journal of Optics*, vol. 16, no. 10, p. 105 009, 2014. DOI: 10.1088/2040-8978/16/10/105009